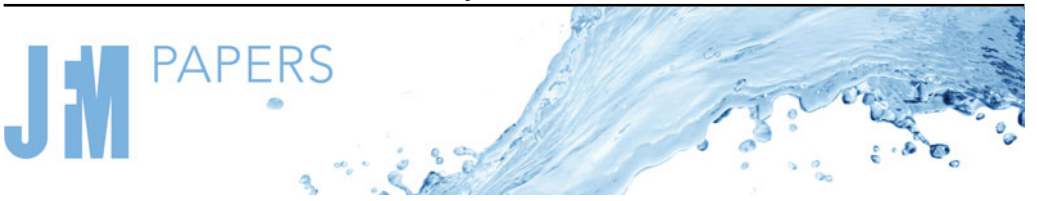
*J. Fluid Mech.* (2025), *vol.* 1015, A28, doi:10.1017/jfm.2025.10351



# Reverse streaming generated by a free-moving magnet

**Aldo Figueroa**[1,3], **Saúl Piedra**[2], **Miguel Piñeirua**[3] and **Sergio Cuevas**[4]

[1]Secihti-Centro de Investigación en Ciencias, Universidad Autónoma del Estado de Morelos, Av. Universidad 1001 Chamilpa, Cuernavaca 62209, Morelos, Mexico

[2]Secihti-Centro de Ingeniería y Desarrollo Industrial, Querétaro De Arteaga 76125, Mexico

[3]Institut de Recherche sur la Biologie de l'Insecte, Université de Tours, Parc de Grandmont, Tours 37200, France

[4]Instituto de Energías Renovables, Universidad Nacional Autónoma de México, Temixco, Morelos 62580, Mexico

**Corresponding author:** Aldo Figueroa, alfil@uaem.mx

(Received 16 December 2024; revised 27 May 2025; accepted 3 June 2025)

Generation of steady streaming vortices is usually accomplished by mechanically vibrating bodies, as occurs in several microfluidic applications for mixing, as well as for transport and handling of microparticles. Here, we propose the generation of streaming from the harmonic electromagnetic forcing of a free-moving circular magnet held afloat on a shallow electrolytic layer, and show that the sense of rotation of steady vortices is the opposite to that of the classical streaming flow. Reverse streaming is attributed to the coupling between the fluid and the free-moving body. Analytical solutions offer a physical rationale for the observed flow dynamics, while numerical simulation reproduces the experimental observations satisfactorily.

**Key words:** vortex dynamics, MHD and electrohydrodynamics

## 1. Introduction

The creation of a steady vortex motion from a primary oscillatory flow about a vanishing mean produced by oscillating boundaries or a pulsating pressure is known as steady streaming (Schlichting 1955; Riley 2001). This is a second-order effect originated by Reynolds stresses whose nonlinearity causes the flow oscillations in the inner layer to not average zero, giving rise to a net steady flow. This classic topic has received increasing attention in recent decades due to interesting microfluidic applications that rely mainly on

© The Author(s), 2025. Published by Cambridge University Press. This is an Open Access article, distributed under the terms of the Creative Commons Attribution-NonCommercial licence (https://creativecommons.org/licenses/by-nc/4.0/), which permits non-commercial re-use, distribution, and reproduction in any medium, provided the original article is properly cited. The written permission of Cambridge University Press or the rights holder(s) must be obtained prior to any commercial use.



https://doi.org/10.1017/jfm.2025.10351 Published online by Cambridge University Press

the use of acoustic methods to produce streaming (Wiklund, Green & Ohlin 2012). For example, acoustic waves have been proposed to promote streaming in microchannels with the aim of enhancing mixing (Sritharan *et al.* 2006; Ahmed *et al.* 2009) or manipulating suspended particles (Zhang, Minten & Rallabandi 2024), since solid particles trapped in an acoustic standing wave have been observed to undergo propulsion (Li *et al.* 2024). In turn, streaming eddies produced by fluid oscillation in a microchannel containing a fixed cylinder have been used to trap and suspend cells without surface contact (Lutz, Chen & Schwartz 2006), while particle sorting has been achieved by streaming flows generated by microbubbles (Thameem, Rallabandi & Hilgenfeldt 2017). The use of streaming flows for the transport and handling of microparticles, control of particle flocculation (Kleischmann *et al.* 2024), even driving untethered mobile robots, aims at bioengineering and healthcare processes such as drug delivery (Ceylan *et al.* 2017; Parthasarathy, Chan & Gazzola 2019). In order to illustrate the effects of body elasticity on streaming, Bhosale, Parthasarathy & Gazzola (2022) investigated oscillatory flow around a submerged soft cylinder. They found that soft bodies promote streaming effects at frequencies significantly lower than rigid bodies, which the authors call soft streaming and speculate that biological creatures could take advantage of soft streaming because of their softness. Following the same steps as the two-dimensional calculation around the soft cylinder made by Bhosale *et al.* (2022), the same team performed a three-dimensional derivation around an immersed soft sphere (Cui, Bhosale & Gazzola 2024). This elaborate derivation opens up a new description of streaming in biological soft environments and robotics (Marmottant 2024). However, the analytical derivations of Cui *et al.* (2024) need to be compared with experiments.

As is usually done macroscopically, streaming production in most previous works relies on the use of immersed bodies, such as cylinders or bubbles, coupled to mechanical or acoustic transducers, which present some limitations. Otherwise, in microfluidic applications, streaming is produced by moving fluid with external pumps. Another possibility that has recently been explored numerically is the use of an oscillating electromagnetic body force produced in a liquid metal layer by an oscillating permanent magnet located underneath the liquid layer (Prinz 2019; Prinz *et al.* 2021). The numerical results show the generation of steady streaming, which has been used in an optimisation problem where randomly distributed massless particles are advected by the flow to achieve a homogeneous distribution while keeping the work done to move the permanent magnet minimal.

Here, we propose a reliable alternative based on the free-oscillating motion of a magnetised body in a conducting fluid driven by electromagnetic forces. We used the interaction of an electric current with the magnetic field created by a magnet floating on an electrolyte to produce a Lorentz force that gives rise to a vortex dipole with a jet-like flow in the central part. The jet exerts a hydrodynamic force that accelerates the floating magnet as if it were a self-propelled body, grabbing the fluid with a volumetric force that overcomes the drag force on the solid magnet. Recently, it has been shown that a small magnet that moves freely on the surface of an electrolyte can be displaced by injecting an electric current into the fluid (Piedra *et al.* 2018, 2023). Using the versatility of electromagnetic forcing, if an alternating current is injected into a quiescent fluid, then the magnet is set to oscillating motion (see figure 1). We show experimentally, numerically and analytically that the periodic motion of the freely oscillating magnet produces a steady streaming flow that, unexpectedly, is in the opposite direction to that of the classical streaming flow. Since most physiological fluids are electrically conducting, this opens up the possibility of implementing this method for biological applications.



https://doi.org/10.1017/jfm.2025.10351 Published online by Cambridge University Press

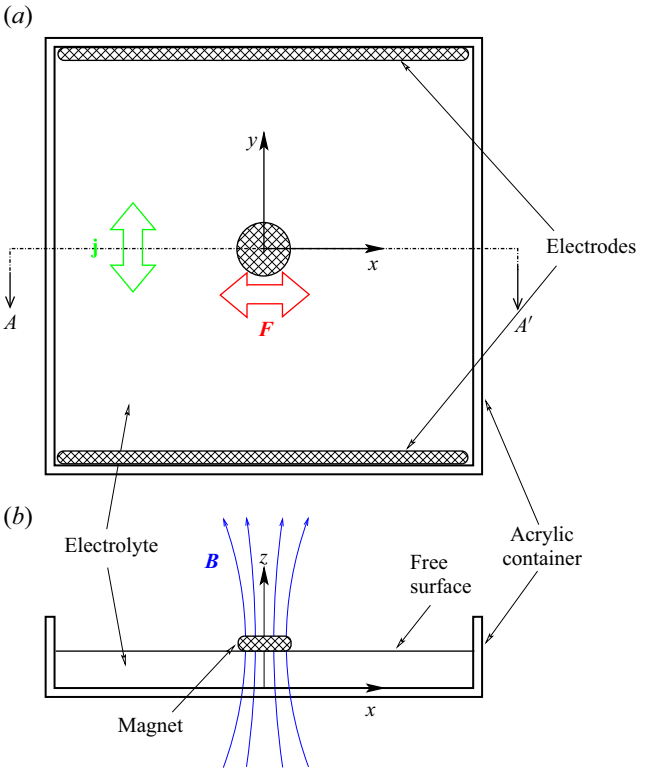



Figure 1. Sketch of the experimental device, not drawn to scale: (*a*) plan view, (*b*) lateral view. The magnetic field $\boldsymbol{B}$ is generated by a floating magnet on the surface of the fluid layer. The AC electric current density $\boldsymbol{j}$ is injected through a pair of copper electrodes. The oscillating Lorentz force is denoted by $\boldsymbol{F}$.

## 2. Experimental model

We used a square acrylic container of length 18 cm; see figure 1. The container was filled with a 0.5 cm layer of an electrolytic solution of potassium chloride (KCl) at 20 % by weight, whose mass density, kinematic viscosity and electrical conductivity are $\rho_f = 1.09 \times 10^3\ \mathrm{kg\,m^{-3}}$, $\nu = 10^{-6}\ \mathrm{m^2\,s^{-1}}$ and $\sigma = 30.9\ \mathrm{S\,m^{-1}}$, respectively. The magnet has a cylindrical shape with diameter 4 mm and maximum magnetic field strength $B_o = 0.165$ T. It was kept afloat on the surface of the electrolyte layer by sticking it to a circular plastic film 6.3 mm in diameter. An extended description of similar experimental set-ups can be found in Piedra *et al.* (2018, 2023). A sinusoidal current is injected through the pair of electrodes, interacting with the magnetic field distribution to generate a Lorentz force that sets the fluid in motion. Subsequently, the flow interacts with the floating magnet, and vice versa. The AC current is obtained from a Stanford Research System DS345 function generator that produces voltage $\pm 20$ V at frequencies in the range 1 μHz to 30.2 MHz, with frequency resolution 1 μHz. Five different frequencies were explored, namely $f = 10$, 30, 50, 100 and 200 mHz, which correspond to the oscillatory Reynolds number values $R_\omega = \omega d^2/\nu = 2.5$, 7.5, 12.5, 25 and 50, where $\omega = 2\pi f$ is the angular frequency of the forcing, and $d = 6.3$ mm is the diameter of the plastic film, which is attached to the magnet to keep it afloat. The magnitude of the electric current, 50 mA, was kept constant for all experiments. The dynamics of the system was recorded at 24 fps with a high-definition Nikon D84 with resolution $1920 \times 1080$ pixels. The velocity field measurements were obtained with particle image velocimetry (PIV). Hollow spherical



https://doi.org/10.1017/jfm.2025.10351 Published online by Cambridge University Press

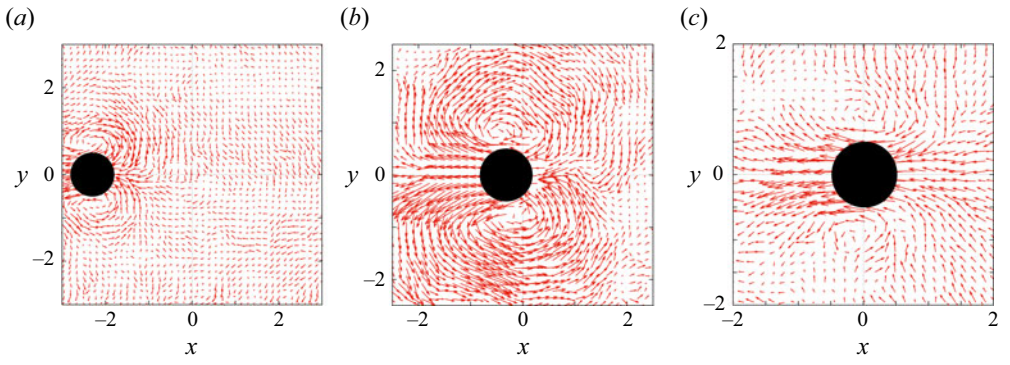



Figure 2. Instantaneous velocity fields from PIV observations: (*a*) $R_\omega = 2.5$, (*b*) $R_\omega = 12.5$, (*c*) $R_\omega = 25$. The black disk denotes the free-moving magnet. The time instants closely correspond to the maximum displacement of the floating magnet. For velocity scales, see figure 3.

glass particles (10 μm in diameter) were seeded on the free surface of the electrolyte layer and illuminated using LEDs. The recorded images were analysed using PIVLab (Thielicke & Stamhuis 2014). Figure 2 shows the experimental velocity fields of PIV on the free electrolyte surface for three different frequencies of the AC current, namely $f = 10$, 50 and 100 mHz. The time instants closely correspond to the maximum displacement $l$ of the floating magnet within its oscillatory dynamics. This displacement is measured on the centroid of the tracked magnet.

## 3. Numerical model

The mathematical model is based on the immersed boundary method (IBM) described in Piedra *et al.* (2018, 2023). The IBM has been proven to be reliable for computing the dynamics of fluid–particle interaction leading to steady streaming of one or two mobile particles (Kleischmann *et al.* 2024). The main idea is to use an indicator field ($I$) to mark the cells where the solid is localised. The mass and momentum equations are solved, coupled with the rigid solid body equations to compute both the fluid flow and the solid body dynamics (Domínguez *et al.* 2021). The indicator field is defined using a Heaviside step function (Tryggvason, Scardovelli & Zaleski 2011). Details about the numerical treatment for the updating of $I$ are reported in Piedra *et al.* (2015, 2018). Once the indicator field is calculated, the velocity $\boldsymbol{u}$ in any cell in the computational domain can be calculated by $\boldsymbol{u}(\boldsymbol{x}) = I(\boldsymbol{x})\,\boldsymbol{u}_f(\boldsymbol{x}) + (1 - I(\boldsymbol{x}))\,\boldsymbol{u}_s(\boldsymbol{x})$, where the subscripts $f$ and $s$ denote the fluid and solid regions, respectively. In general, for conductive fluids subject to electromagnetic forces, the solution of magnetohydrodynamics (MHD) equations becomes imperative. However, in scenarios involving weak electrolytes whose electrical conductivity is very small compared to that of liquid metals, the induced effects are negligible, and the flow can be treated as hydrodynamic with a known external Lorentz force (Figueroa *et al.* 2009). This approach allows us to solve the following mass and momentum equations for the whole domain, accounting for variable density and viscosity:

$$\boldsymbol{\nabla} \cdot \boldsymbol{u} = 0, \tag{3.1}$$

$$\frac{\partial(\rho \boldsymbol{u})}{\partial t} + \boldsymbol{\nabla} \cdot (\rho \boldsymbol{u}\boldsymbol{u}) = -\boldsymbol{\nabla} p + \boldsymbol{\nabla} \cdot \mu(\boldsymbol{\nabla}\boldsymbol{u} + \boldsymbol{\nabla}^{\mathrm{T}}\boldsymbol{u}) + I(\boldsymbol{j}^0 \times \boldsymbol{B}^0), \tag{3.2}$$

where $\boldsymbol{u}$ is the velocity field, $p$ is the pressure, $\boldsymbol{B}^0$ is the magnetic field produced by the permanent magnet, $\boldsymbol{j}^0$ is the applied current density, $\rho$ is the mass density, and $\mu$ is the



https://doi.org/10.1017/jfm.2025.10351 Published online by Cambridge University Press

dynamic viscosity. The Lorentz force term in the momentum equations is multiplied by the indicator function since this force exclusively influences the fluid region. The velocity derived from the momentum equations may not inherently satisfy the rigidity condition within the solid region. Consequently, the velocity field, determined by the flow solver, is integrated across the solid domain to ascertain the velocity of the centroid and the angular velocity of the body:

$$M_s \boldsymbol{u}_{sc}^{n+1} = \int (1 - I)\rho_s \boldsymbol{u} \, \mathrm{d}V, \tag{3.3}$$

$$\boldsymbol{I}_s \Omega_z^{n+1} = \int (1 - I)\boldsymbol{r} \times \rho_s \boldsymbol{u} \, \mathrm{d}V, \tag{3.4}$$

where $M_s$ is the mass of the solid, $\boldsymbol{u}_{sc}$ is the velocity of the centroid of the solid, $\boldsymbol{I}_s$ is the moment of inertia tensor, and $\Omega_z$ is the angular velocity. After computing the translational and angular velocities of the solid body, the corrected velocity field within the solid region ($\boldsymbol{u}_s$) is determined by $\boldsymbol{u}_s = \boldsymbol{u}_{sc} + \boldsymbol{r} \times \Omega_z \hat{k}$, where $\boldsymbol{r}$ is the position vector, i.e. the distance to any point inside the solid from the centre of rotation of the rigid body. As the solid moves through the fluid, the properties of the material within the domain, including density and viscosity, depend on position and time. Consequently, they must be calculated at each time step to accurately capture the evolving dynamics of the system. Calculating any material property ($\alpha$) can be performed through the indicator field

$$\alpha(\boldsymbol{x}, t) = \alpha_s(1 - I(\boldsymbol{x}, t)) + \alpha_f \, I(\boldsymbol{x}, t). \tag{3.5}$$

To obtain a dimensionless version of the mass and momentum equations, it is convenient to introduce the following dimensionless variables:

$$\boldsymbol{x}^* = \frac{\boldsymbol{x}}{d}, \quad \boldsymbol{u}^* = \frac{\boldsymbol{u}}{u_o}, \quad \rho^* = \frac{\rho}{\rho_f}, \quad p^* = \frac{p}{\rho_f u_o^2}, \quad \mu^* = \frac{\mu}{\mu_f},$$
$$\boldsymbol{j}^{0*} = \frac{\boldsymbol{j}^0}{j_0}, \quad \boldsymbol{B}^{0*} = \frac{\boldsymbol{B}^0}{B_0}, \quad t^* = \omega t, \tag{3.6}$$

where $d$ is the diameter of the plastic film, $u_o = \nu_f / d$ is the characteristic viscous velocity, and $j_0$ and $B_0$ are the magnitudes of the electric current density and the magnetic field, respectively. Additionally, to take into account the friction of the fluid with the bottom of the container, we use a quasi-two-dimensional approach (Q2D) that involves the averaging of the equations in the $z$-direction, normal to the free surface. Then the averaged mass and momentum balance equations are expressed in dimensionless form as

$$\nabla \cdot \boldsymbol{u} = 0, \tag{3.7}$$

$$R_\omega \frac{\partial(\rho \boldsymbol{u})}{\partial t} + \nabla \cdot (\rho \boldsymbol{u}\boldsymbol{u}) = -\nabla p + \nabla \cdot \mu(\nabla \boldsymbol{u} + \nabla^T \boldsymbol{u}) - \frac{\boldsymbol{u}}{\tau} + Q I(\boldsymbol{j}^0 \times \boldsymbol{B}^0), \tag{3.8}$$

where the superscript $^*$ has been omitted. More details on obtaining non-dimensional equations and numerical implementation can be found in our previous study (Piedra *et al.* 2018). The third term in (3.8) denotes Rayleigh friction, with $\tau$ representing the characteristic time scale for vorticity damping due to dissipation in the viscous layers. This term arises from the $z$-directional averaging of the conservation equations (Figueroa *et al.* 2009), and the expression for computing $\tau$ is provided in Piedra *et al.* (2018). The flow is governed by the oscillatory Reynolds number $R_\omega = \omega d^2/\nu$, and the Lorentz force parameter $Q = U_0/u_0$. The characteristic bulk velocity $U_0 = j_0 B_0 d^2/\rho_f \nu_f$ is obtained from a balance between the viscous and applied Lorentz forces (see Figueroa



https://doi.org/10.1017/jfm.2025.10351 Published online by Cambridge University Press

*et al.* 2009). As in Piedra *et al.* (2018, 2023), the normal component of the magnetic field $B_z(x, y)$ was modelled by a Gaussian distribution that approximates very closely the distribution of a small magnetic dipole (Cuevas, Smolentsev & Abdou 2006).

In the Q2D numerical model, the solid body submerged in the fluid is represented as a circular surface, with diameter denoted by $d$. This diameter specifically corresponds to the size of the plastic film responsible for keeping the magnet afloat in the fluid. The Lorentz force parameter for all simulations is $Q = 2640$, which corresponds to the experimental conditions. In addition, the other characteristic parameter of the flow is the ratio of solid and fluid densities, $\rho_r = \rho_s/\rho_f$, which remains constant in our simulations, equal to 0.677. The numerical code considers the entire experimental domain that was discretised in a regular grid of $764 \times 764$ control volumes in the $x$- and $y$-directions, respectively. The time step was set to $10^{-4}$ for all simulations to yield consistent results. For the initial condition, the fluid is assumed to be quiescent, and the velocity satisfies the free-slip conditions at the boundaries of the container. The boundaries are away from the core flow by at least a distance of ten diameters of the plastic disk, thus their effect on the vortex formation can be considered negligible. The numerical code has been successfully validated in previous studies (Piedra *et al.* 2018, 2023; Domínguez *et al.* 2021).

## 4. Analytical model

Let us now address the problem of the free-moving dipole magnet with a different approach. Instead of considering a solid floating magnet, we envisage the field generated by a fixed point magnetic dipole (Cuevas *et al.* 2006) in a conducting fluid layer set in oscillating motion. This is a simplified version of the problem addressed numerically by Prinz (2019) and Prinz *et al.* (2021), but considering a change in the reference system. In fact, the flow generated in a conducting fluid layer by the field of an oscillating magnet has also been treated by Beltrán *et al.* (2010), although the streaming flow was not explored. Thus the physical model described in § 2 is addressed using the MHD approximation for mathematical modelling purposes. The governing equations are formulated in terms of the induced magnetic field, which is known as the $b$-formulation. Furthermore, the low magnetic Reynolds number approximation ($R_m \ll 1$) is used since it is appropriate for electrolyte and liquid metal MHD flows at laboratory and industrial scales (Müller & Bühler 2001), where $R_m = \mu_0 \sigma U d$, $\mu_0$ and $U$ being the vacuum magnetic permeability and the characteristic upstream flow velocity. This approximation implies that the magnetic field induced by the fluid motion is much weaker than the applied magnetic field. In dimensionless terms, the system of governing equations reads as follows:

$$\boldsymbol{\nabla} \cdot \boldsymbol{u} = 0, \tag{4.1}$$

$$R_\omega \frac{\partial \boldsymbol{u}}{\partial t} + Re\,(\boldsymbol{u} \cdot \boldsymbol{\nabla})\,\boldsymbol{u} = -\boldsymbol{\nabla} p + \boldsymbol{\nabla}^2 \boldsymbol{u} + Ha^2 \left(\boldsymbol{j}^i \times \boldsymbol{B}^0\right), \tag{4.2}$$

$$\boldsymbol{\nabla}^2 \boldsymbol{b} = (\boldsymbol{u} \cdot \boldsymbol{\nabla})\,\boldsymbol{B}^0, \tag{4.3}$$

$$\boldsymbol{j}^i = \boldsymbol{\nabla} \times \boldsymbol{b}, \tag{4.4}$$

where velocity $\boldsymbol{u}$, pressure $p$, induced electric current density $\boldsymbol{j}^i$, applied magnetic field $\boldsymbol{B}^0$, and induced magnetic field $\boldsymbol{b}$ have been normalised by $u_0$, $\rho u_0^2$, $\sigma U B_0$, $B_0$ and $R_m B_0$, respectively. The spatial coordinates are normalised by the characteristic length $d$, which is taken as the diameter of the magnet, and the time $t$ is normalised with the angular frequency $\omega$ of the forcing. The dimensionless parameters involved are the hydrodynamic



https://doi.org/10.1017/jfm.2025.10351 Published online by Cambridge University Press

Reynolds number $Re = Ud/\nu$, the oscillatory Reynolds number $R_\omega = \omega d^2/\nu$, and the Hartmann number $Ha = B_0 d(\sigma/\rho\nu)^{1/2}$, respectively. The square of the latter is the ratio of magnetic to viscous forces. Equations (4.1)–(4.4) are the continuity equation, the Navier–Stokes equation with the Lorentz force term, the induction equation that under this approximation reduces to a Poisson equation for the induced magnetic field, and Ampère's law, respectively. Additionally, the applied magnetic field $\boldsymbol{B}^0$ satisfies the magnetostatic equations $\boldsymbol{\nabla} \cdot \boldsymbol{B}^0 = 0$ and $\boldsymbol{\nabla} \times \boldsymbol{B}^0 = 0$, which ensures its solenoidal and irrotational character.

With the aim of getting analytical solutions of (4.1)–(4.4), we introduce some simplifying assumptions. First, we assume that the flow is two-dimensional and takes place in an infinite domain. Therefore, the effects of the bottom wall and the free surface are ignored. Under these conditions, only the component of the applied magnetic field normal to the plane of motion is relevant, namely $B_z^0(x, y)$. With these assumptions, the governing equations reduce to

$$\frac{\partial u}{\partial x} + \frac{\partial v}{\partial y} = 0, \tag{4.5}$$

$$R_\omega \frac{\partial u}{\partial t} + Re\left(u\frac{\partial u}{\partial x} + v\frac{\partial u}{\partial y}\right) = -\frac{\partial p}{\partial x} + \nabla_\perp^2 u + Ha^2\, j_y^i B_z^0, \tag{4.6}$$

$$R_\omega \frac{\partial v}{\partial t} + Re\left(u\frac{\partial v}{\partial x} + v\frac{\partial v}{\partial y}\right) = -\frac{\partial p}{\partial y} + \nabla_\perp^2 v - Ha^2\, j_x^i B_z^0, \tag{4.7}$$

$$\nabla_\perp^2 b_z = u\frac{\partial B_z^0}{\partial x} + v\frac{\partial B_z^0}{\partial y}, \tag{4.8}$$

$$j_x = \frac{\partial b_z}{\partial y}, \quad j_y = -\frac{\partial b_z}{\partial x}, \tag{4.9}$$

where the subscript $\perp$ indicates the projection of the $\boldsymbol{\nabla}$ operator on the $(x, y)$-plane.

### 4.1. *Boundary conditions*

We assume that far from the magnetic dipole, an oscillatory uniform flow in the positive $x$-direction is imposed. With the origin of coordinates located at the point of maximum magnetic field strength, the boundary conditions on the velocity components are

$$u(x, y) \to \sin(t), \quad v(x, y) \to 0 \quad \text{as } x, y \to \pm\infty. \tag{4.10}$$

It is obviously expected that the strength of the induced magnetic field is higher near the zone where the applied magnetic field is strong. As the distance from the source of the applied field grows, the induced field must decrease and vanish at infinity. Therefore, it must satisfy

$$b_z(x, y) \to 0 \quad \text{as } x, y \to \pm\infty. \tag{4.11}$$

### 4.2. *Applied and induced magnetic field*

In order to linearise the equations of motion, we assume that the flow past the magnetic point dipole is only slightly perturbed by the Lorentz force produced by the interaction of the induced electric currents with the applied field. Hence the dimensionless velocity components can be expressed as

$$u(x, y) = \sin(t) + u'(x, y), \quad v(x, y) = v'(x, y), \tag{4.12}$$



https://doi.org/10.1017/jfm.2025.10351 Published online by Cambridge University Press

where $u'$ and $v'$ are the perturbations of the background oscillating flow due to the presence of the magnetic dipole. Assuming that $u', v' < 1$, and neglecting the products of the field derivatives with $u'$ and $v'$, the magnetic induction equation (4.8) reduces to

$$\nabla_\perp^2 b_z = \frac{\partial B_z^0}{\partial x} \sin(t). \tag{4.13}$$

Notice that this equation is uncoupled from the velocity perturbations. In this approximation, the induced field $b_z$ is generated by an oscillating unperturbed flow. This equation can be integrated analytically if the applied magnetic field $B_z^0$ is assumed to be a point magnetic dipole. The normal component of a two-dimensional point magnetic dipole located at the origin, with its magnetic dipole moment pointing in the positive $z$-direction, can be expressed as (Cuevas *et al.* 2006)

$$B_z^0(x, y) = \frac{1}{2\pi} \frac{1}{x^2 + y^2} + \delta(x)\, \delta(y). \tag{4.14}$$

Hence the solution of (4.13) is

$$b_z(x, y) = \frac{x}{2\pi (x^2 + y^2)} \sin(t), \tag{4.15}$$

and the components of the induced electric current density, $j_x^i$ and $j_y^i$, can be calculated from (4.9), namely

$$j_x^i(x, y) = -\frac{xy}{\pi (x^2 + y^2)^2} \sin(t), \quad j_y^i(x, y) = \frac{(x - y)(x + y)}{2\pi (x^2 + y^2)^2} \sin(t). \tag{4.16}$$

Due to the nature of the applied magnetic field, namely the magnetic point dipole, the solution (4.15) and components (4.16) diverge at the origin.

### 4.3. *Asymptotic solutions*

Taking the curl of (4.6)–(4.7), we get the following vorticity transport equation for the only component $\omega_z$:

$$R_\omega \frac{\partial \omega_z}{\partial t} + Re \left( u \frac{\partial \omega_z}{\partial x} + v \frac{\partial \omega_z}{\partial y} \right) = \nabla_\perp^2 \omega_z - Ha^2 \left( j_x^i \frac{\partial B_z^0}{\partial x} + j_y^i \frac{\partial B_z^0}{\partial y} \right), \tag{4.17}$$

where $\omega_z = \partial v/\partial x - \partial u/\partial y$ is the vorticity in the $z$-direction. We now seek an asymptotic solution as a double perturbation expansion for small values of the parameters $Re$ and $R_\omega$. First, we expand the vorticity $\omega_z$ (and similarly the velocity components $u$, $v$) as a series in integral powers of $Re$, i.e.

$$\omega_z = \omega_z^{(0)} + Re\, \omega_z^{(1)} + Re^2\, \omega_z^{(2)} + \mathcal{O}(Re^3), \tag{4.18}$$

where the superscript denotes the order of the approximation. Solutions of this sort become increasingly accurate as the perturbation parameter $Re$ gets smaller. At zeroth order ($\mathcal{O}(Re^0)$), the vorticity satisfies

$$R_\omega \frac{\partial \omega_z^{(0)}}{\partial t} = \nabla_\perp^2 \omega_z^{(0)} - Ha^2 \left( j_x^i \frac{\partial B_z^0}{\partial x} + j_y^i \frac{\partial B_z^0}{\partial y} \right). \tag{4.19}$$

Now we expand the vorticity (and the velocity components) as a series in the small parameter $R_\omega$, i.e.

$$\omega_z^{(0)} = \omega_z^{(0,0)} + R_\omega\, \omega_z^{(0,1)} + R_\omega^2\, \omega_z^{(0,2)} + \mathcal{O}\big(R_\omega^3\big). \tag{4.20}$$



https://doi.org/10.1017/jfm.2025.10351 Published online by Cambridge University Press

The equation of order $\mathcal{O}(Re^0, R_\omega^0)$ satisfies (quasi-steady limit)

$$\nabla_\perp^2 \omega_z^{(0,0)} = Ha^2 \left( j_x^i \frac{\partial B_z^0}{\partial x} + j_y^i \frac{\partial B_z^0}{\partial y} \right). \tag{4.21}$$

Here, with the aim of arriving at simple analytical solutions, instead of (4.14), the normal component of the applied magnetic field is approximated by means of the Gaussian distribution (Cuevas *et al.* 2006; Figueroa, Cuevas & Ramos 2017):

$$B_z^0(x, y) = \frac{\eta}{\pi} \mathrm{e}^{-\eta(x^2+y^2)}. \tag{4.22}$$

Considering $\eta > 0$, (4.22) represents a two-dimensional Gaussian-like magnetic distribution for the normal component. The solution of (4.21) can be approximated as

$$\omega_z^{(0,0)} = \frac{\eta\, Ha^2}{4\pi^2} \frac{y}{x^2+y^2} \sin(t). \tag{4.23}$$

Observe that $\lim_{x,y\to\infty} \omega_z^{(0,0)} = 0$, and that although solution (4.23) presents a singularity at the origin, it correctly reproduces the vorticity in the neighbourhood of the origin. The velocity field can be obtained through the stream function $\psi$, defined as $u = \partial\psi/\partial y$, $v = -\partial\psi/\partial x$, which satisfies the equation

$$\nabla_\perp^2 \psi = -\omega_z. \tag{4.24}$$

By expanding the stream function and vorticity to the zeroth order in $Re$ and the zeroth order in $R_\omega$, (4.24) becomes

$$\nabla_\perp^2 \psi^{(0,0)} = -\omega_z^{(0,0)}, \tag{4.25}$$

whose solution is

$$\psi^{(0,0)} = y \sin(t) - \frac{Ha^2}{32\pi^2 C_0} \frac{y}{x^2+y^2} \sin(t). \tag{4.26}$$

Using the same methodology, the following solutions can be obtained on higher orders for $R_\omega$:

$$\psi^{(0,1)} = -\frac{2Ha^2}{768\pi^2 C_0 \eta} \frac{y}{x^2+y^2} \cos(t), \tag{4.27}$$

$$\psi^{(0,2)} = \frac{6Ha^2}{36\,864\pi^2 C_0 \eta^2} \frac{y\,\mathrm{e}^{-\eta(x^2+y^2)}}{x^2+y^2} \sin(t), \tag{4.28}$$

$$\psi^{(1,0)} = \frac{Ha^2\, R_\omega^2 xy \sin(t) \left(12\,288\, C_0\pi^2 \sin(t) - Ha^2 \left(4-(x^2+y^2)\eta\right) \left(R_\omega \cos(t) + 24\eta \sin(t)\right)\right)}{37\,748\,736\,\pi^4 C_0 C_1 (x^2+y^2)\eta^2}. \tag{4.29}$$

The constants $\eta$, $C_0$, and $C_1$ have the values $\eta = 0.05$, $C_0 = 0.04$, $C_1 = 0.5$. Finally, the approximate solution reads

$$\psi(x, y, t) = Re^0 \left( R_\omega^0 \psi^{(0,0)} + R_\omega^1 \psi^{(0,1)} + R_\omega^2 \psi^{(0,2)} \right) + Re^1 \left( R_\omega^0 \psi^{(1,0)} \right). \tag{4.30}$$

Note that solution (4.30) considers small nonlinear effects. The divergence at $r \to 0$ and $r \to \infty$ reveals a problem intrinsic to the approximation $Re \ll 1$. However, as shown in figure 3, the solution (4.30) provides a suitable approximation at intermediate regions.



https://doi.org/10.1017/jfm.2025.10351 Published online by Cambridge University Press

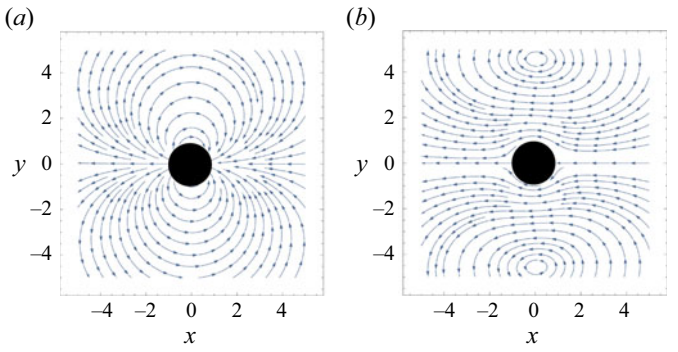



Figure 3. Instantaneous velocity fields: (*a*) $R_\omega = 0.1$, (*b*) $R_\omega = 0.9$. The black disk denotes the free-moving magnet. Analytic calculations from (4.30).

When the oscillatory Reynolds number is very small, the magnetic obstacle promotes two recirculation zones; see figure 3(*a*). However, as $R_\omega$ increases, the vortices are detached perpendicularly to the direction of motion, as seen in figure 3(*b*). A similar dynamics is found with an oscillating cylinder in a quiescent fluid when the oscillations have a very small amplitude (Pradeep & Ashoke 2021), or the two-dimensional flow produced by the harmonic oscillation of a magnetic obstacle in a quiescent viscous, electrically conducting fluid (Beltrán *et al.* 2010; Prinz 2019).

## 5. Results

Initially, the magnet remains static in the quiescent fluid. The flow starts when the electric current is injected and interacts with the magnetic field of the floating magnet, producing a Lorentz force in the $x$-direction. The Lorentz force promotes a vortex dipole with the floating magnet at its centre, as reported by Piedra *et al.* (2018, 2023). The jet-like flow in the central part of the vortex dipole exerts a hydrodynamic force that accelerates the floating magnet. As the electric current is alternating, it changes direction, and the magnet moves in the negative $x$-direction, following the generated flow. In this way, the magnet maintains an oscillating motion along the $x$-axis.

Figure 2 shows the experimental snapshots of the PIV velocity fields for three different forcing frequencies. As seen in figure 2, the maximum dimensionless displacement $D = l/d$ of the oscillating magnet is reduced as the frequency increases. It is greater than 2.0 for $R_\omega = 2.5$, less than 1.0 for $R_\omega = 12.5$, and less than 0.5 for $R_\omega = 25$. By tracking the motion of the magnet, a maximum velocity $U = 0.8$ mm s$^{-1}$ was reached for $R_\omega = 2.5$. With this velocity scale, the Reynolds number is $Re = Ud/\nu = 5$, which corresponds to a laminar flow regime around the free-moving body. We must note that the analytical results for the oscillating magnetic dipole in figure 3(*b*) qualitatively agree with the experimental observation for the high forcing frequencies in figures 2(*b*) and 2(*c*), where $D$ is smaller than unity. Although the analytical model comes from a different physical situation, namely the interaction of an oscillating conducting fluid with a localised magnetic field, rather than a fluid–structure interaction as in the experiment, it correctly captures the dynamics of the experiment for low $Re$ and high $R_\omega$, i.e. the detachment of vortices in the $y$-direction.

The dynamics of the experimental system is presented in figure 4, where the Reynolds number $Re$ and the maximum dimensionless displacement $D$ are plotted as functions of the oscillatory Reynolds number $R_\omega$. This figure comprises results obtained



https://doi.org/10.1017/jfm.2025.10351 Published online by Cambridge University Press

experimentally, numerically and analytically. Numerical results were obtained from the fluid–structure interaction approach based on the IBM with a Q2D approximation that accounts for the bottom friction, as described in § 3. Taking into account that the flows analysed are in the laminar regime ($Re \leqslant 5$), the dynamics of the floating magnet can also be approached in a simplified analytical way. The total force acting on the free-moving magnet is

$$\boldsymbol{F} = \boldsymbol{F}_L + \boldsymbol{F}_d, \tag{5.1}$$

where $\boldsymbol{F}_L$ is the Lorentz force promoted by the applied electric current and the magnetic field produced by the magnet, namely $\boldsymbol{F}_L = \int_V (\boldsymbol{j}^0 \times \boldsymbol{B}^0)\, \mathrm{d}V$, while $\boldsymbol{F}_d$ is the drag force. Even though the magnet presents a cylindrical geometry, as a first approximation, the latter frictional force can be calculated from the Stokes formula for the drag on a spherical object moving in a viscous fluid at small Reynolds numbers, i.e. $\boldsymbol{F}_d = -6\pi\,\mu\, R\boldsymbol{u}$ (Stokes drag), where $R$ is the radius of the magnet. Considering that only the component of the applied magnetic field normal to the plane of motion is relevant, namely $B_z^0 = B_0$, and that the applied electric current is on the $y$-axis, i.e. $j_y^0 = j_0 \cos(\omega t)$, the magnet's motion is unidirectional, i.e. it moves in the $x$-axis with velocity $u_m$. In dimensional terms, the equation of motion of the magnet driven by the oscillatory electromagnetic forcing under a linear viscous drag is

$$V_s \rho_s \frac{du_m}{dt} = V_f\, j_0 B_0 \cos(\omega t) - 6\pi\,\mu\, R u_m, \tag{5.2}$$

where $Vs$ and $V_f$ denote the volume of the solid and the volume of the displaced fluid, respectively. Considering that these volumes are approximately the same, $V_f \approx V_s$, (5.2) can be written in dimensionless form as

$$R_\omega \frac{\mathrm{d}u_m}{\mathrm{d}t} = \frac{1}{\rho_r}\left(Q\cos(t) - u_m\right), \tag{5.3}$$

where $Q$ is the previously defined Lorentz force parameter, and $\rho_r = \rho_s/\rho_f$ is the density ratio between the floating solid and the fluid. Note that the density ratio arises due to the fluid–structure interaction between the electromagnetically driven flow and the floating magnet.

The general solution of (5.3) is the sum of a transient solution that depends on the initial conditions and a harmonic steady-state solution. The latter solution reads

$$u_m(t) = \frac{Q}{\left(1 + R_\omega^2 \rho_r^2\right)^{1/2}} \cos(t + \phi), \tag{5.4}$$

where $\phi = -\arctan(R_\omega \rho_r)$ is the phase between the electromagnetic force and the moving magnet. Furthermore, the position of the free-moving magnet can be obtained by integrating (5.4):

$$x_m(t) = \frac{Q}{\left(1 + R_\omega^2 \rho_r^2\right)^{1/2}} \sin(t + \phi). \tag{5.5}$$

From (5.5), we can infer that for fixed $Q$, the maximum displacement of the magnet is proportional to the amplitude of $x_m$, i.e. $D \sim (1 + R_\omega^2 \rho_r^2)^{-1/2}$. Similarly, from (5.4), the maximum velocity of the magnet $U$ is proportional to the amplitude of $u_m$, thus $Re \sim (1 + R_\omega^2 \rho_r^2)^{-1/2}$. Experimentally, the density ratio is $\rho_r = 0.8$. In figure 4, the results obtained experimentally, as well as from numerical and analytical procedures, show that



https://doi.org/10.1017/jfm.2025.10351 Published online by Cambridge University Press

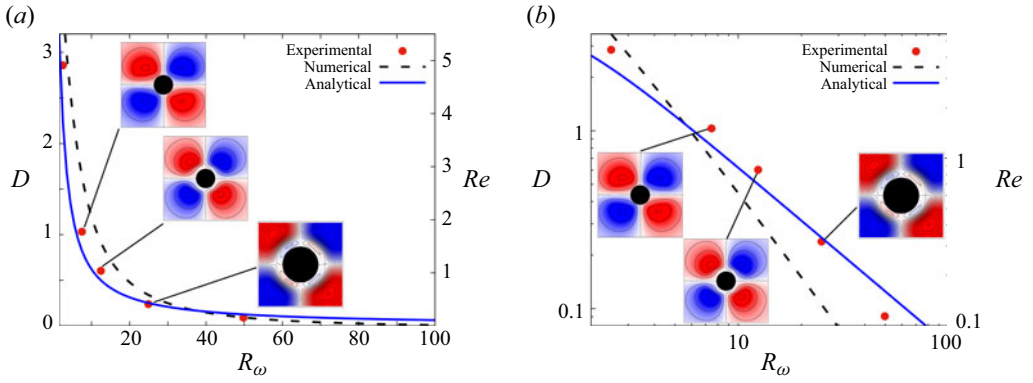



Figure 4. (*a*) Dimensionless amplitude $D$ and Reynolds number $Re$ as functions of the oscillation Reynolds number $R_\omega$. (*b*) A log-log plot. Markers indicate experimental observations. Continuous line indicates theoretical approximation from (5.4). Dashed line indicates numerical simulations. In the streaming maps obtained numerically, the red and blue colours denote positive and negative rotation, respectively, and correspond, from left to right, to $R_\omega = 7.5$, $R_\omega = 12.5$ and $R_\omega = 25$. The black disk in the streaming maps denotes the free-moving magnet.

both $D$ and $Re$ dramatically decrease asymptotically to zero with $R_\omega$. In fact, Q2D numerical simulations agree well qualitatively and quantitatively with the experimental data. Furthermore, considering the forcing $Q$ as constant, the amplitudes in (5.4)–(5.5) decrease as $R_\omega$ increases, qualitatively describing the experimental data.

Figure 4 also shows the numerically calculated streamlines for the streaming flows generated by the oscillatory magnet. The streaming was calculated by time-averaging the flows in one oscillation period $T = 1/f$. The red and blue colours in the streaming maps denote positive and negative rotation, respectively. For low frequency, $R_\omega = 7.5$, viscous effects dominate over inertia so that a Stokes-like steady streaming flow (Bhosale, Parthasarathy & Gazzola 2020) is obtained, characterised by a four-vortex structure around the magnet, as has been found in experimental (Lieu, House & Schwartz 2012) and numerical (Bhosale *et al.* 2020) studies. A transition region is found for $R_\omega = 12.5$, in which the boundary layers around the magnet begin to change the topology of the streaming flow. In this case, the small-amplitude oscillations ($D \leqslant 1$) generate a Stokes layer of thickness $\delta = R_\omega^{-1/2} = 0.28$, which coincides with the numerical work of Bhosale *et al.* (2020). For large frequencies, $R_\omega \geqslant 25$, the interplay of inertial and viscous effects leads to the formation of a double boundary layer. The inner layer, also known as the DC boundary layer, has thickness $\delta_{DC} = 0.67$, which coincides with the numerical value calculated by Parthasarathy *et al.* (2019). Moreover, it has been reported that in terms of the streaming Reynolds number $Rs = \omega l^2/\nu$, where $l$ is the maximum displacement of the magnet (see figure 2), the eight-vortex structure is found for $Rs \sim \mathcal{O}(1)-\mathcal{O}(10)$ (Bhosale *et al.* 2020). Incidentally, the calculated value in our case is $Rs = 1.35$.

Focusing on the eight-vortex structure, figure 5 shows the streaming velocity field for the numerical simulation (left quadrant) and the experimental PIV observations (right quadrant) for $R_\omega = 25$. Under these conditions, the magnet performs small-amplitude oscillations ($D \leqslant 1$), and the Reynolds number is lower than unity ($Re = 0.7$). In the numerical result, we observe a large external vortex interacting with a smaller internal vortex close to the free-moving magnet. For the sake of clarity, the numerical results (left quadrant) are plotted with only a quarter of the data. Due to the poor resolution of the experimental data (right quadrant), we can only observe the large external vortex with rotation opposite to its corresponding one in the left quadrant, but it depicts a



https://doi.org/10.1017/jfm.2025.10351 Published online by Cambridge University Press

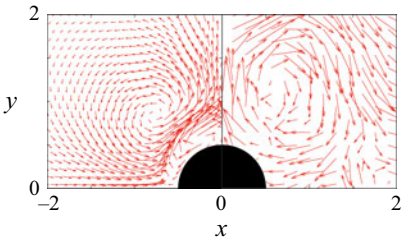



Figure 5. Streaming velocity field for $R_\omega = 25$. Left quadrant: numerical simulation. Right quadrant: experimental PIV observation. The black disk denotes the free-moving magnet. For velocity scale, see figure 4.

similar streaming structure. Inner and outer flow recirculations have been obtained in analytical (Wang 1968) and numerical (Elston, Blackburn & Sheridan 2006) studies. They were also observed experimentally by Masakazu Tatsuno (Van Dyke 1982). In the case of an infinitely long smooth circular cylinder in an infinite extent of fluid, the problem is usually analysed with two dimensionless control parameters, namely the Keulegan–Carpenter number $KC = Re/\beta$, and the Stokes number $\beta = d^2/\nu T$. The flow conditions corresponding to the steady streaming structure observed by Tatsuno were characterised by $KC = 0.54$ and $\beta = 5$ (An, Cheng & Zhao 2009). Consequently, the parameters for the streaming structure with eight vortices seen in figures 4 and 5 are close to those of Tatsuno, namely, $KC = 0.18$ and $\beta = 3.9$. Although three-dimensional effects may appear in these flows, the present experiments were carried out under conditions where Q2D behaviour prevails. Even though the streaming flows in our study present a pattern similar to previously reported vortical structures, there is a significant difference that must be highlighted. For the eight-vortex structure, the streaming flow is in the opposite direction since the outer recirculation is directed towards the body along the axis of oscillation, i.e. a reverse streaming is observed.

### 5.1. *Modified Stokes' second problem with a free-moving wall*

The reverse streaming can be attributed to a phase shift between the electromagnetically driven motion of the fluid and the free-moving magnet. In order to better understand the reverse streaming, we first consider a simplified case, namely, a wall under an oscillating free stream (Panton 2024), which we refer to as the modified Stokes' second problem. The latter can be applied to our problem if we focus on the side wall (edge) of the floating magnet, and consider this surface as an infinite flat plate with the reference frame $(x'-y')$ located at its surface. While the Stokes problem considers the flow created by an oscillating solid wall above which a viscous fluid exists, the modified Stokes problem considers a far-field flow oscillating over a stationary wall located at $y' = 0$, as shown in figure 6. The dimensionless velocity $u_S$ for this flow reads as

$$u_S(y', t) = \cos(t) - \mathrm{e}^{-y'/\delta}[\cos(t - y'/\delta)], \tag{5.6}$$

where $\delta = (2/R_\omega)^{1/2}$ is the Stokes boundary layer. If the rigid wall is allowed to move freely, then the shear stress promoted by the oscillating flow with velocity $u_S$, namely $\tau_s = (\mathrm{d}u_S/\mathrm{d}y')|_{y'=0}$, drives the wall in the oscillation direction, as shown in figure 6(*a*). Therefore, the equation of motion of the rigid flat wall located at $y' = 0$ reads as

$$R_\omega \frac{\mathrm{d}u_w}{\mathrm{d}t} = \frac{1}{\rho_r}\left(\tau_s - u_w\right), \tag{5.7}$$



https://doi.org/10.1017/jfm.2025.10351 Published online by Cambridge University Press

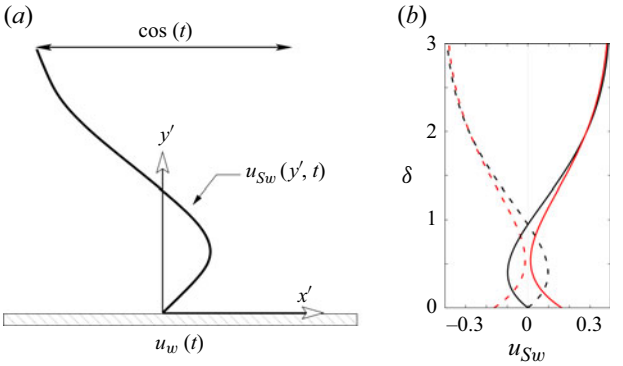



Figure 6. (*a*) Sketch of the modified Stokes' second problem where a far-field flow oscillates (as cos($t$)) on top of a rigid flat wall free to move with velocity $u_w$ located at $y' = 0$. (*b*) Velocity profiles from an oscillating stream field $u_{Sw}$ (see (5.10)). Black lines indicate $\rho_r = 10$ ($u_w = 0$, i.e. fixed wall). Red lines indicate $\rho_r = 0.8$ ($u_w \neq 0$, i.e. free-moving wall). Continuous lines indicate $t = \pi/\sqrt{7}$. Dashed lines indicate $t = \pi + \pi/\sqrt{7}$. Here, $R_\omega = 50$.

where $u_w$ is the velocity of the free-moving wall. Note that the first and second terms on the right-hand side of (5.7) refer to the shear stress and the linear drag, respectively. It can be shown that the solution to (5.7) is

$$u_w(t) = c\cos(t + \varphi), \tag{5.8}$$

where the amplitude $c$ of the oscillation and the phase shift $\varphi$ are given as

$$c = \left(\frac{R_\omega}{1 + R_\omega^2 \rho_r^2}\right)^{1/2}, \quad \varphi = \arctan\left(\frac{1 - R_\omega \rho_r}{1 + R_\omega \rho_r}\right). \tag{5.9}$$

Equations (5.8) and (5.9) show that there is a phase shift $\varphi$ between the oscillatory far-field flow and the rigid wall, and that this phase shift is a function of the density ratio $\rho_r$ and the oscillatory Reynolds number $R_\omega$. Thus combining (5.6) and (5.8), the modified Stokes' second problem with a free-moving wall at $y' = 0$ is

$$u_{Sw}(y', t) = \cos(t) - \mathrm{e}^{-y'/\delta}[\cos(t - y'/\delta) - c\cos(t - y'/\delta + \varphi)]. \tag{5.10}$$

The effect of the oscillatory fluid on the free-moving wall depends on the dimensionless parameters $R_\omega$ and $\rho_r$. From (5.10), evaluating at $y' = 0$, we obtain the velocity of the wall $u_w(t)$, i.e. (5.8). When $R_\omega = 1/\rho_r$, the maximum amplitude of the wall's velocity is obtained ($c = 1/\sqrt{2\rho_r}$), and the phase shift is zero ($\varphi = 0$). In turn, when both $\rho_r$ and $R_\omega$ are large, the amplitude approaches $c \approx 0$. In this case, the density of the wall is larger than that of the fluid, $\rho_r > 1$. Thus the shear stress caused by the flow is not sufficient to displace the wall, and the modified Stokes' second problem with the wall at rest is recovered, namely (5.6); see the black lines in figure 6(*b*). On the other hand, for small $\rho_r$ and large $R_\omega$, which corresponds to the experimental case ($\rho_r = 0.8$, $R_\omega = 50$), the wall oscillates with amplitude and phase shift $c \approx R_\omega^{-1/2}$ and $\varphi \approx -\pi/4$, respectively, as observed with the red lines in figure 6(*b*). Hence when the density of the wall is smaller than that of the fluid, $\rho_r < 1$, there is a phase shift between the oscillating fluid and the rigid wall. In fact, comparing continuous or dashed lines of the velocity profiles for $\rho_r > 1$ and $\rho_r < 1$ in figure 6(*b*), a change of sign appears in the velocity profile inside the boundary layer.



https://doi.org/10.1017/jfm.2025.10351 Published online by Cambridge University Press

### 5.2. *Reverse streaming*

To summarise § 5.1, if a submerged solid object is allowed to move freely in an oscillatory flow and $\rho_r < 1$, then the shear stress on the object is significant, causing it to oscillate with a phase shift $\varphi$ relative to the oscillatory far-field flow. In this case, the velocity profile changes sign inside the boundary layer, which can promote reverse streaming. Returning to the problem of the free-moving dipole magnet, in order to introduce the phase shift in the stream function of the analytic solution (4.30), we modify the corresponding boundary condition (4.10) in the form $u(x, y) \to \sin(t + \varphi)$. The solution is then averaged over one oscillation period to obtain the streaming flow $\Psi_S$, which can be approximated as

$$\Psi_S(x, y) = \frac{1}{2\pi} \int_0^{2\pi} \psi(x, y, t)\, \mathrm{d}t \approx \frac{xy(60(1 - (x^2 + y^2)\eta) - 5\pi^2)\cos(\varphi - \pi/2)}{\pi^4 \eta^2 (x^2 + y^2)^2\, \mathrm{e}^{(x^2+y^2)\eta}}. \tag{5.11}$$

Compared to previously published analytical solutions of steady streaming induced by vibrating cylinders or spheres (Raney, Corelli & Westervelt 1954; Riley 1965, 1967, 1975*a*,*b*; Wang 1965, 1968; Stuart 1966; Tabakova & Zapryanov 1982; Longuet-Higgins 1998; Ilin & Sadiq 2010; Bhosale *et al.* 2022; Cui *et al.* 2024), the simplicity of (5.11) is noteworthy, as it also takes into account reverse streaming. This equation is valid for $-\pi/4 \leqslant \varphi \leqslant \pi/4$. In (5.11), the phase shift can be approximated as $\varphi \approx \arctan((1 - \rho_r)/(1 + \rho_r))$. Therefore, when the density ratio is $\rho_r > 1$, the phase shift varies in the range $-\pi/4 \leqslant \varphi < 0$, and conventional streaming is found. For $\rho_r = 1$, the phase shift is $\varphi = 0$ and the streaming flow is zero ($\Psi_S(x, y) = 0$). Finally, for $\rho_r < 1$, the range of phase change variation is $0 < \varphi \leqslant \pi/4$ and the streaming flow is reversed. Figure 7 shows the streaming flows calculated from (5.11) and from numerical simulation. The conventional streaming is observed for $\varphi = -\pi/4$, where the streaming flow in the outer recirculation is directed away from the body along the oscillation axis; see figure 7(*a*). In contrast, for $\varphi = \pi/4$, reverse streaming is obtained, as observed in figure 7(*b*). This flow structure coincides qualitatively with the numerical and experimental results presented in figures 4 and 5. Note that if the averaging procedure is taken directly to the solution (4.30), then the ordinary streaming is obtained, as found numerically in Prinz (2019) and Prinz *et al.* (2021). Additionally, numerical simulations reproduce the classic streaming of an oscillating rigid cylinder and the reverse streaming from the free-moving magnet (see figures 7*c*,*d*), which qualitatively agree with the analytical solution (5.11). We must note that since the realistic system does not comply with the simplifications used to derive the analytical solution (5.11), the comparison with numerical results can be only qualitative. Furthermore, we also note that the Stokes drift must be taken into account for (4.30) in order to calculate real trajectories followed by particles inside the oscillatory flow (Lane 1955; Bhosale *et al.* 2022).

In particle hydrodynamic studies in acoustic fields, steady streaming has been observed to promote particle propulsion (Li *et al.* 2024; Zhang *et al.* 2024), and reversal in the propulsion direction at a distinct frequency. The reversal is attributed to the oscillatory rotation of the spherical particle with the rectilinear oscillation of the surrounding fluid. The reversal in propulsion occurs at $R_\omega = 29.08$ (Li *et al.* 2024). The latter value almost coincides with when the reverse streaming is observed in figure 4 ($R_\omega = 25$). Although the problem analysed by Li *et al.* (2024) is different from ours, since Li *et al.* (2024) consider a spherical particle trapped in an acoustic standing wave, the reversal propulsion could be linked to reverse streaming.

https://doi.org/10.1017/jfm.2025.10351 Published online by Cambridge University Press

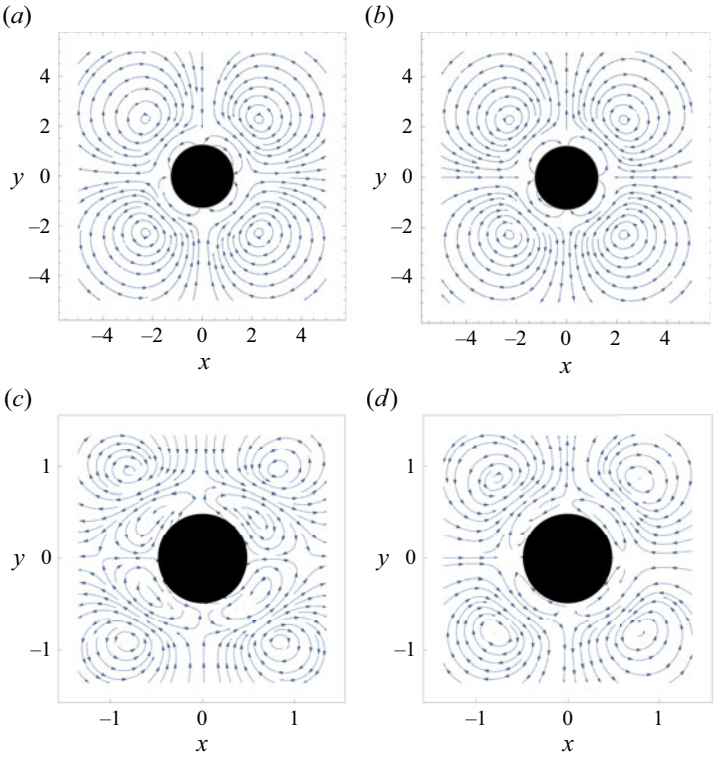



Figure 7. Streaming flow calculated from (5.11): (*a*) conventional streaming ($\varphi = -\pi/4$); (*b*) reverse streaming ($\varphi = \pi/4$). Streaming flow calculated numerically: (*c*) streaming from an oscillating cylinder ($\rho_r > 1$), $R_\omega = 150$; (*d*) reverse streaming from an oscillating free-moving magnet ($\rho_r < 1$), $R_\omega = 25$. The black disk denotes the free-moving magnet or cylinder.

## 6. Concluding remarks

We have demonstrated for the first time the feasibility of promoting steady streaming flows through electromagnetic forcing of a freely oscillating magnetic dipole floating in a shallow electrolytic layer. In contrast to the classical case where an infinitely long circular cylinder oscillates harmonically in an unbounded quiescent fluid, or a fixed cylinder is immersed in an oscillatory harmonic flow, the streaming flow generated by the freely oscillating magnet is in the opposite direction, which means that the outer recirculation is directed towards the body along the axis of oscillation. The cause of the reverse streaming is a phase shift resulting from the free-moving boundary. To explain the appearance of the phase shift, it was first shown in the modified Stokes' second problem where a viscous fluid oscillates on top of a free-moving rigid wall. A similar procedure was then applied to the analytic solution of the oscillating flow of a magnetic point dipole in a conducting fluid, from which the stream function of the streaming flow was obtained. In the proper limits, according to the density ratio of the object to the fluid, this solution recovers the ordinary steady streaming flow as well as the reverse streaming. The reverse streaming phenomenon is expected to be independent of the method used to produce the flow oscillation; therefore, in principle, it could be detected with a freely oscillating particle in an acoustic field.

A future study could consider the inclusion of perpendicular electric currents for off-axis motion, as described in Figueroa *et al.* (2017). The potential applications of steady streaming as a robust mechanism for achieving flow and passive particle control



https://doi.org/10.1017/jfm.2025.10351 Published online by Cambridge University Press

in a regime associated with emerging miniaturised robotic applications such as drug delivery are promising. In this regard, reverse streaming should be taken into account for future investigations, regardless of the method of generating the flow, as it could affect the control of the flow and passive particles. In addition, because of the electrical conductivity of most physiological fluids, the possibility of using electromagnetic forces to induce oscillatory motion of small magnetised objects and eventually streaming could be considered for medical and biological applications. Taking factors such as biodegradability and biocompatibility into account, magnetised objects could be more suitable for medical procedures in microenvironments.

**Acknowledgements.** A.F. and S.P. thank the Investigadoras e Investigadores por México programme from Secihti, Mexico. A.F. also thanks Université de Tours for financial support during his sabbatical leave at Institut de Recherche sur la Biologie de l'Insecte.

**Funding.** This research was supported by Fundación Marcos Moshinsky and the Universidad Nacional Autónoma de México (DGAPA IN107921).

**Declaration of interests.** The authors report no conflict of interest.

## References

Ahmed, D., Mao, X., Shi, J., Juluri, B.K. & Huang, T.J. 2009 A millisecond micromixer via single-bubble-based acoustic streaming. *Lab on a Chip* **9** (18), 2738–2741.

An, H., Cheng, L. & Zhao, M. 2009 Steady streaming around a circular cylinder in an oscillatory flow. *Ocean Engng* **36** (36), 1089–1097.

Beltrán, A., Ramos, E., Cuevas, S. & Brøns, M. 2010 Bifurcation analysis in a vortex flow generated by an oscillatory magnetic obstacle. *Phys. Rev. E* **81** (3), 036309.

Bhosale, Y., Parthasarathy, T. & Gazzola, M. 2020 Shape curvature effects in viscous streaming. *J. Fluid Mech.* **898**, A13.

Bhosale, Y., Parthasarathy, T. & Gazzola, M. 2022 Soft streaming – flow rectification via elastic boundaries. *J. Fluid Mech.* **945**, R1.

Ceylan, H., Giltinan, J., Kozielski, K. & Sitti, M. 2017 Mobile microrobots for bioengineering applications. *Lab on a Chip* **17** (10), 1705–1724.

Cuevas, S., Smolentsev, S. & Abdou, M. 2006 Vorticity generation in creeping flow past a magnetic obstacle. *Phys. Rev. E* **74** (5), 056301.

Cui, S., Bhosale, Y. & Gazzola, M. 2024 Three-dimensional soft streaming. *J. Fluid Mech.* **979**, A7.

Domínguez, D.R., Piedra, S. & Ramos, E. 2021 Vortex-induced vibration in a cylinder with an azimuthal degree of freedom. *Phys. Rev. Fluids* **6** (6), 064701.

Elston, J.R., Blackburn, H.M. & Sheridan, J. 2006 The primary and secondary instabilities of flow generated by an oscillating circular cylinder. *J. Fluid Mech.* **550**, 359–389.

Figueroa, A., Cuevas, S. & Ramos, E. 2017 Lissajous trajectories in electromagnetically driven vortices. *J. Fluid Mech.* **815**, 415–434.

Figueroa, A., Demiaux, F., Cuevas, S. & Ramos, E. 2009 Electrically driven vortices in a weak dipolar magnetic field in a shallow electrolytic layer. *J. Fluid Mech.* **641**, 245–261.

Ilin, K. & Sadiq, M. 2010 Steady viscous flows in an annulus between two cylinders produced by vibrations of the inner cylinder. arXiv:1008.4704v2 [physics.flu-dyn]. pp. 1–29.

Kleischmann, F., Luzzatto-Fegiz, P., Meiburg, E. & Vowinckel, B. 2024 Pairwise interaction of spherical particles aligned in high-frequency oscillatory flow. *J. Fluid Mech.* **984**, A57.

Lane, C.A. 1955 Acoustical streaming in the vicinity of a sphere. *J. Acoust. Soc. Am.* **27** (6), 1082–1086.

Li, P., Nunn, A.R., Brumley, D.R., Sader, J.E. & Collis, J.F. 2024 The propulsion direction of nanoparticles trapped in an acoustic field. *J. Fluid Mech.* **984**, R1.

Lieu, V.H., House, T.A. & Schwartz, D.T. 2012 Hydrodynamic tweezers: impact of design geometry on flow and microparticle trapping. *Analyt. Chem.* **21** (4), 1963–1968.

Longuet-Higgins, M.S. 1998 Viscous streaming from an oscillating spherical bubble. *Proc. R. Soc. Lond. A* **33** (4), 344–357.

Lutz, B.R., Chen, J. & Schwartz, D.T. 2006 Hydrodynamic tweezers: 1. Noncontact trapping of single cells using steady streaming microeddies. *Analyt. Chem.* **78** (15), 5429–5435.

Marmottant, P. 2024 Large vortices from soft vibrations. *J. Fluid Mech.* **986**, F1.



https://doi.org/10.1017/jfm.2025.10351 Published online by Cambridge University Press

MÜLLER, U. & BÜHLER, L. 2001 *Magnetofluiddynamics in Channels and Containers*. Springer.
PANTON, R.L. 2024 *Incompressible Flows*, 5th edn. Wiley.
PARTHASARATHY, T., CHAN, F.K. & GAZZOLA, M. 2019 Streaming-enhanced flow-mediated transport. *J. Fluid Mech.* **878**, 647–662.
PIEDRA, S., FLORES, J., RAMÍREZ, G., FIGUEROA, A., PINEIRUA, M. & CUEVAS, S. 2023 Fluid mixing by an electromagnetically driven floating rotor. *Phys. Rev. E* **108** (2), 025101.
PIEDRA, S., RAMOS, E. & HERRERA, J.R. 2015 Dynamics of two-dimensional bubbles. *Phys. Rev. E* **91** (6), 063013.
PIEDRA, S., ROMÁN, J., FIGUEROA, A. & CUEVAS, S. 2018 Flow produced by a free-moving floating magnet driven electromagnetically. *Phys. Rev. Fluids* **3** (4), 043702.
PRADEEP, K.S. & ASHOKE, D. 2021 A robust sharp interface based immersed boundary framework for moving body problems with applications to laminar incompressible flows. *Comput. Maths Appl.* **83**, 24–56.
PRINZ, S. 2019 Direct and large-eddy simulations of wall-bounded magnetohydrodynamic flows in uniform and non-uniform magnetic fields. PhD thesis, Institut für Thermo- und Fluiddynamik, Technische Universität Ilmenau.
PRINZ, S., THOMANN, J., EICHFELDER, G., BOECK, T. & SCHUMACHER, J. 2021 Expensive multi-objective optimization of electromagnetic mixing in a liquid metal. *Optim. Engng* **22** (2), 1065–1089.
RANEY, W.P., CORELLI, J.C. & WESTERVELT, P.J. 1954 Acoustical streaming in the vicinity of a cylinder. *J. Acoust. Soc. Am.* **26** (6), 1006–1014.
RILEY, N. 1965 Oscillating viscous flows. *Mathematika* **12** (2), 161–175.
RILEY, N. 1967 Oscillatory viscous flows. review and extension. *IMA J. Appl. Maths* **3** (4), 419–434.
RILEY, N. 1975*a* The steady streaming induced by a vibrating cylinder. *J. Fluid Mech.* **68** (4), 801–812.
RILEY, N. 1975*b* Unsteady laminar boundary layers. *SIAM Rev.* **17** (2), 274–297.
RILEY, N. 2001 Steady streaming. *Annu. Rev. Fluid Mech.* **33** (1), 43–65.
SCHLICHTING, H. 1955 *Boundary Layer Theory*. McGraw-Hill.
SRITHARAN, K., STROBL, C.J., SCHNEIDER, M.F., WIXFORTH, A. & GUTTENBERG, Z. 2006 Acoustic mixing at low Reynolds numbers. *Appl. Phys. Lett.* **88** (5), 054102.
STUART, J.T. 1966 Double boundary layers in oscillatory viscous flow. *J. Fluid Mech.* **24** (4), 673–687.
TABAKOVA, S.S. & ZAPRYANOV, Z.D. 1982 On the hydrodynamic interaction of two spheres oscillating in a viscous fluid. I. Axisymmetrical case. *Z. Angew. Math. Phys.* **33** (4), 344–357.
THAMEEM, R., RALLABANDI, B. & HILGENFELDT, S. 2017 Fast inertial particle manipulation in oscillating flows. *Phys. Rev. Fluids* **2** (5), 052001(R).
THIELICKE, W. & STAMHUIS, E.J. 2014 PIVlab – towards user-friendly, affordable and accurate digital particle image velocimetry in MATLAB. *J. Open Res. Softw.* **2**, e30.
TRYGGVASON, G., SCARDOVELLI, R. & ZALESKI, S. 2011 *Direct Numerical Simulations of Gas–Liquid Multiphase Flows*, 1st edn. Cambridge University Press.
VAN DYKE, M. 1982 *An Album of Fluid Motion*. Parabolic Press.
WANG, C.-Y. 1965 The flow field induced by an oscillating sphere. *J. Sound Vib.* **2** (3), 257–269.
WANG, C.-Y. 1968 On high-frequency oscillatory viscous flows. *J. Fluid Mech.* **32** (1), 55–68.
WIKLUND, M., GREEN, R. & OHLIN, M. 2012 Acoustofluidics 14: applications of acoustic streaming in microfluidic devices. *Lab on a Chip* **12** (14), 2438–2451.
ZHANG, X., MINTEN, J. & RALLABANDI, B. 2024 Particle hydrodynamics in acoustic fields: unifying acoustophoresis with streaming. *Phys. Rev. Fluids* **9** (4), 044303.

https://doi.org/10.1017/jfm.2025.10351 Published online by Cambridge University Press